

1 **A Consistent Treatment of Microwave Emissivity and Radar Backscatter for**
2 **Retrieval of Precipitation over Water Surfaces**

3 S. Joseph Munchak*

4 *Earth System Science Interdisciplinary Center, University of Maryland, College Park*

5 Robert Meneghini

6 *NASA Goddard Space Flight Center, Greenbelt, MD*

7 Mircea Grecu

8 *Morgan State University, Baltimore, MD*

9 William S. Olson

10 *Joint Center for Earth System Technology, University of Maryland Baltimore County, Baltimore,*
11 *MD*

12 *Corresponding author address: Mesoscale Atmospheric Processes Laboratory, NASA Goddard
13 Space Flight Center, 8800 Greenbelt Rd, Greenbelt, MD 20771.

14 E-mail: s.j.munchak@nasa.gov

ABSTRACT

15 The Global Precipitation Measurement satellite's Microwave Imager (GMI)
16 and Dual-frequency Precipitation Radar (DPR) are designed to provide the
17 most accurate instantaneous precipitation estimates currently available from
18 space. The GPM Combined Algorithm (CORRA) plays a key role in this pro-
19 cess by retrieving precipitation profiles that are consistent with GMI and DPR
20 measurements; therefore it is desirable that the forward models in CORRA
21 use the same geophysical input parameters. This study explores the feasi-
22 bility of using internally consistent emissivity and surface backscatter cross
23 section (σ_0) models for water surfaces in CORRA. An empirical model for
24 DPR Ku and Ka σ_0 as a function of 10m wind speed and incidence angle is
25 derived from GMI-only wind retrievals under clear conditions. This allows
26 for the σ_0 measurements, which are also influenced by path-integrated atten-
27 uation (PIA) from precipitation, to be used as input to CORRA and for wind
28 speed to be retrieved as output. Comparisons to buoy data give a wind rmse
29 of 3.7 m/s for Ku+GMI and 3.2 m/s for Ku+Ka+GMI retrievals under precip-
30 itation (compared to 1.3 m/s for clear-sky GMI-only), and there is a reduction
31 in bias from the GANAL background data (-10%) to the Ku+GMI (-3%) and
32 Ku+Ka+GMI (-5%) retrievals. Ku+GMI retrievals of precipitation increase
33 slightly in light (< 1 mm/hr) and decrease in moderate to heavy precipitation
34 (> 1 mm/hr). The Ku+Ka+GMI retrievals, being additionally constrained by
35 the Ka reflectivity, increase only slightly in moderate and heavy precipitation
36 at low wind speeds (< 5 m/s) relative to retrievals using the surface reference
37 estimate of PIA as input.

38 1. Introduction

39 Algorithms for estimating precipitation from space-borne radars at attenuating frequencies (e.g.,
40 TRMM PR (Iguchi et al. 2000, 2009), CloudSat (Mitrescu et al. 2010), GPM DPR (Grecu et al.
41 2011)) have long realized the benefit of an estimate of the path-integrated attenuation (PIA) that is
42 independent of the reflectivity profile for the purposes of constraining the integrated and surface
43 precipitation amount. In general, such an estimate of the PIA is obtained via a form of the sur-
44 face reference technique (SRT; (Meneghini et al. 2000, 2004)), which subtracts the surface radar
45 backscatter cross-section (σ_0) in a precipitating column from a precipitation-free reference. The
46 difference is then assumed to be due to attenuation from precipitation after accounting for multiple
47 scattering (Battaglia and Simmer 2008) and the effect of precipitation on the surface itself (Seto
48 and Iguchi 2007). If the ratio of this difference to the uncertainty in the reference value, known
49 as the reliability factor, is large, then the precipitation retrieval is more strongly constrained, be-
50 cause the PIA is sensitive to the vertically-integrated third moment of the particle size distribution
51 whereas the reflectivity is sensitive to the sixth moment.

52 Algorithms that make simultaneous use of passive microwave and radar data (Haddad et al.
53 1997; Grecu et al. 2004; Munchak and Kummerow 2011) generally use the SRT PIA along with
54 microwave radiances to constrain the precipitation profile (indeed, PIA can be the dominant con-
55 straint because of its high resolution relative to the passive microwave footprint, especially when
56 the reliability factor is large). These algorithms also require knowledge of the surface emissiv-
57 ity in order to forward model the brightness temperatures for comparison to observations. Since
58 emission and reflection are related processes, it is logical for a combined algorithm to exploit
59 any relationships between σ_0 and emissivity that may exist. Over water surfaces, it is known
60 that wind-induced surface roughness and foam have a large impact on σ_0 and emissivity; thus, it

61 should benefit a combined algorithm to retrieve the 10m wind speed in order to achieve internal
62 consistency between the forward-modeled PIA and brightness temperatures.

63 The purpose of this work is not only to highlight the benefits of unifying the active and passive
64 surface characteristics for the purpose of precipitation retrievals from GPM, but also to demon-
65 strate the feasibility of combined DPR-GMI retrievals of surface wind over water, particularly
66 when precipitation is present. This has historically been problematic for both passive and active
67 (scatterometer) wind retrievals (Weissman et al. 2012), despite the high motivation to develop ca-
68 pabilities to monitor the strength of tropical and extratropical cyclones. For passive measurements,
69 higher frequency channels (> 19 GHz) can become opaque to the surface in rain and clouds, and
70 although the surface emission is not fully obscured at lower frequencies, measurements at multiple
71 frequencies near the C-band are required to distinguish the surface and rain column contributions
72 to the observed radiances (Uhlhorn et al. 2007). However, the large footprints that are character-
73 istic of spaceborne microwave radiometers at these frequencies are not optimal for retrievals of
74 wind and precipitation due to non-uniformity within the footprint. Even outside of rain, cross-
75 talk between wind, water vapor and cloud liquid water can bias wind retrievals (O'Dell et al.
76 (2008); Rapp et al. (2009)). Also, rain creates an additional source of surface waves, which can
77 either enhance or damp surface backscatter, depending on angle, frequency, and wind speed (Stiles
78 and Yueh (2002), Seto and Iguchi (2007)). Backscattering from the rain itself can also enhance
79 the measured surface cross-section, particularly for scatterometers that are designed to maximize
80 signal-to-noise ratio by employing relatively long pulse widths and large footprint sizes (Li et al.
81 2002). Finally, in high winds the sensitivity of σ_0 to wind speed is low (Donnelly et al. (1999);
82 Fernandez et al. (2006)), limiting the accuracy of retrievals even if rain effects are accounted for.

83 As of yet, only the short-lived Midori-II AMSR-SeaWinds combination of passive and active
84 instruments have been designed specifically for the measurement of ocean winds, but several in-

85 vestigators have taken advantage of existing platforms with these measurements (e.g., TRMM and
86 Aquarius) or coincident overpasses of scatterometer and passive microwave radiometers to eluci-
87 date further information about the atmosphere and sea state than is possible from either instrument
88 type alone. Studies based on the TRMM microwave imager (TMI) and precipitation radar (PR)
89 have often used the TMI-based wind retrievals as a reference to develop geophysical model func-
90 tions (GMFs) for PR, which relate wind speed and σ_0 (e.g., Li et al. (2002); Freilich and Vanhoff
91 (2003); Tran et al. (2007)). These are then used to retrieve the wind field independently with PR
92 (Li et al. 2004) either as a standalone product or for use as a reference to estimate the rain-induced
93 attenuation as an input to the rainfall estimation algorithms. In the case of WindSat, a comparison
94 of its retrievals and QuickScat wind vectors in coincident overpasses was performed by Quilfen
95 et al. (2007), who found differences between the two depended on wind speed and water vapor (a
96 consequence of the aforementioned cross-talk between parameters). The authors also attempted to
97 combine the two sets of measurements via multiple regression. They found that adding QuickScat
98 to WindSat did not improve wind retrievals outside of rain, but they did note a slight improve-
99 ment under raining conditions. More recently, the Aquarius satellite, which offers active and
100 passive measurements at L-band for the purpose of ocean salinity retrieval, was launched. Yueh
101 et al. (2013) developed GMFs based on SSM/I and NCEP reanalysis collocations and found that
102 the resulting combined active-passive retrievals of wind speed and salinity compared favorably to
103 salinity retrievals where ancillary data was used to set the wind vector.

104 The growing number of satellites with active and passive microwave instruments (e.g., TRMM,
105 GPM, Aquarius, SMAP), along with airborne platforms (e.g., the NASA Global Hawk Hurricane
106 and Severe Storm Sentinel-HS3) represents an opportunity to use these combinations to retrieve
107 ocean winds, particularly under conditions (such as rain) where single-sensor methods are under-
108 constrained. This study is based on data from the Global Precipitation Measurement (GPM) satel-

lite, which has a particularly useful set of measurements for developing the GMFs due to the well-calibrated, high resolution GPM Microwave Imager (GMI) instrument (Draper et al. 2015) and a dual-frequency precipitation radar (DPR) which improves the capability to separate surface effects from rain-induced attenuation. Our strategy (Figure 1) is to develop a GMF for DPR based upon co-located GMI wind retrievals, and then use this GMF under raining conditions by modifying the combined GPM DPR-GMI precipitation retrieval algorithm CORRA (Olson and Masunaga 2015). In order to have as accurate a wind reference as possible, we evaluate three emissivity models after calculating offsets under clear and calm conditions to achieve consistency with the GMI calibration. Next, we use all available matchups of GMI and DPR under non-precipitating conditions to develop the GMFs. This process is presented in section 2. Next, the use of GMFs in the GPM combined GMI-DPR ensemble filter retrieval framework, including validation of winds in regions of precipitation against buoy measurements, is described in section 3, followed by a summary in section 4.

2. Development of Geophysical Model Functions for DPR

Although physical models exist to describe the relationship between wind speed, the wave spectrum, and backscatter (Durden and Vesecky (1985); Majurec et al. (2014)), the desire for GPM applications is to be as internally consistent as possible between the emissivity model and DPR GMF. Therefore, the strategy in this study is to derive empirical GMFs from clear-sky matchups of DPR and GMI-derived 10m wind retrievals, eliminating as much as possible the error from precipitation and cloud cross-talk described in section 1, then apply those GMFs to retrievals under all conditions. The use of empirical GMFs derived in this manner is standard practice in the scatterometer community (Migliaccio and Reppucci 2006).

131 The first step in this process is to generate the clear-sky wind retrievals and then assess their error
 132 relative to buoy observations. In the absence of precipitation, the microwave radiances measured
 133 by GMI are primarily sensitive to the surface emission, atmospheric temperature and water vapor
 134 profile, and cloud liquid water. These parameters can be solved for using optimal estimation, also
 135 known as variational, retrieval techniques. These have been implemented for microwave sensors
 136 by Elsaesser and Kummerow (2008) and Boukabara et al. (2011), and a blend of their approaches is
 137 used to derive the surface and atmospheric properties from GMI by minimizing the cost function:

$$J = (\mathbf{x} - \mathbf{x}_a)^T \mathbf{S}_x^{-1} (\mathbf{x} - \mathbf{x}_a) + (\mathbf{y} - f(\mathbf{x}))^T \mathbf{S}_y^{-1} (\mathbf{y} - f(\mathbf{x})). \quad (1)$$

138 The components of the optimal estimation retrieval are the state vector (\mathbf{x}) and covariance ma-
 139 trix (\mathbf{S}_x), the observation vector (\mathbf{y}) and covariance matrix (\mathbf{S}_y), and forward model $f(\mathbf{x})$. For
 140 water surfaces, the state vector consists of the 10m wind speed, cloud liquid water path, and a
 141 set of variables representing the values of the leading empirical orthogonal functions (EOFs) of
 142 the atmospheric temperature and water vapor profile. These EOFs were derived from 10 years
 143 of MERRA reanalysis (Rienecker et al. (2011); NASA/GMAO (2008)) independently in 1K SST
 144 bins. The number of leading EOFs is chosen such that at least 99% of the variance in temperature
 145 and water vapor is explained by the selected EOFs. The EOFs are used to simultaneously adjust
 146 the initial atmospheric temperature and water vapor profiles in order to match the observed GMI
 147 radiances. This is a change from the Elsaesser and Kummerow (2008) method, which assumed a
 148 constant lapse rate and scale height for water vapor. These assumptions are sufficient for matching
 149 observations near the 22-GHz water vapor absorption line, where radiances are mostly sensitive to
 150 the total column-integrated amount of water vapor and are less sensitive to its vertical structure and
 151 emitting temperature. However both the vertical structure of water vapor and temperature matter
 152 for modeling the additional channels near 183 GHz on GMI, so some method of adjusting the

153 shape of the profile in mid and upper levels is necessary. The EOFs represent the climatological
154 co-varying structures in temperature and water vapor profiles, and are a robust way to adjust both
155 without requiring temperature sounding channels (e.g., 50-55 GHz). The *a priori* (and initial) state
156 \mathbf{x}_a is the MERRA reanalysis interpolated in time and space to the GMI pixel location.

157 Because the atmosphere is represented by EOFs and no covariance between the atmosphere and
158 wind/cloud is assumed, the state covariance matrix \mathbf{S}_x is diagonal. The observation vector consists
159 of the 13-channel GMI radiances from the GMI Level 1C-R (intercalibrated and co-located) prod-
160 uct (GPM Science Team 2015). The co-location matches the high-frequency (HF) observations
161 (166V&H, 183 ± 3 , and 183 ± 7 GHz), which are observed at 49.2° earth incidence angle, with the
162 lower-frequency (LF) observations, which are observed at 52.8° earth incidence angle. A diagonal
163 matrix for \mathbf{S}_y is also assumed, with values of instrument noise (Hou et al. 2014) plus additional
164 error determined from buoy matchups (Table 1) to account for forward model error and inexact
165 footprint matching.

166 The forward model is derived from the Community Radiative Transfer Model (CRTM) Emis-
167 sion (non-scattering atmosphere) model, modified to include the downwelling path length cor-
168 rection for roughened water surfaces as described by Meissner and Wentz (2012) and using the
169 same atmospheric layers that are provided by MERRA products up to 10 hPA. Absorption by at-
170 mospheric gases is calculated from Rosenkranz (1998) and Tretyakov et al. (2003). Cloud liquid
171 absorption follows Liebe et al. (1991) and cloud water is assumed to follow an adiabatic profile
172 (Albrecht et al. 1990). Since the surface emissivity and its relationship to wind speed is of funda-
173 mental importance to this study, three emissivity models were tested for their ability to produce
174 unbiased clear-sky radiances when forced with buoy-observed surface winds (within 30 minutes
175 of a GPM overpass) and MERRA atmospheric profiles: FASTEM4/5 (as implemented in CRTM;

176 Liu et al. (2011)) and the Meissner and Wentz (2012) (hereafter MW) model.¹ Wind direction
 177 was not considered in this study as only the MW model is capable of representing wind direction-
 178 induced emissivity changes. Instead we include the wind-direction induced error in total model
 179 error which is derived from buoy matchups. The source of wind observations in this study is the
 180 International Comprehensive Ocean-Atmosphere Data Set version 2.5 (ICOADS; Woodruff et al.
 181 (2011); NCDC/NESDIS/NOAA (2011, updated monthly)) from April 2014-March 2015. Only
 182 observations from platforms with a known anemometer height (h_b) were considered, and all winds
 183 were adjusted to 10m assuming neutral buoyancy using the relationship (Hsu et al. 1994):

$$w_{10} = w_b(10/h_b)^{0.11}. \quad (2)$$

184 Before the emissivity models can be intercompared, sensor calibration must be considered. Fol-
 185 lowing Meissner and Wentz (2012), a calm-wind offset (δ_0) was determined for each emissivity
 186 model and each GMI channel. These offsets were obtained by first selecting a subset of ICOADS
 187 observations with 10m winds less than 3.5 m s^{-1} , where the emissivity-wind relationship is linear.
 188 To filter out clouds, observations were excluded if the polarization difference at 89 GHz was less
 189 than an SST-dependent threshold representing a cloud liquid water path of 0.01 kg m^{-2} under
 190 average atmospheric conditions or the spatial standard deviation (within 15 km) of 89 GHz Tb
 191 was greater than 2 K. The RTM was then forced with the observed SST and wind speed and in-
 192 terpolated MERRA atmospheric profile. The offsets were then calculated in order to minimize the
 193 bias between observed and simulated GMI brightness temperatures. No offsets were applied to
 194 the 183 GHz channels, as these were not sensitive to the surface emissivity in the matchups. The
 195 offsets and root-mean-square error (after offsets have been applied) are given for each channel
 196 and emissivity model in Table 1. The biases are different for each model at low frequencies, but
 197 similar or identical at 166 GHz, indicating low sensitivity of the brightness temperatures to emis-

¹Note that the MW model does not include frequencies higher than 90 GHz and FASTEM5 was substituted at these frequencies.

sivity at these channels and therefore low confidence in the offsets, which are likely influenced by the water vapor absorption model and/or absolute calibration of GMI. The root-mean-square-error (rmse) values, which are not sensitive to the choice of emissivity model, represent the error from other components of the forward model (such as wind direction and water vapor absorption) plus instrument noise, and are used as the diagonal components of \mathbf{S}_y .

Next, each emissivity model was evaluated under the full range of conditions encountered in the GMI buoy overpasses. The retrieval was performed with each emissivity model and the retrieved winds are compared with observations in Figure 2. These results were filtered to remove precipitation by applying a maximum threshold of 1.0 for the normalized cost function. It is apparent from these results that the MERRA analysis is biased high at observed wind speeds below 3 m s^{-1} and biased low above this threshold. The retrievals using the different emissivity models behave similarly to each other up to about 8 m s^{-1} and remove most of this bias, but diverge due to different foam models (implicit in MW and explicit in FASTEM 4/5). At observed wind speeds greater than 15 m s^{-1} , FASTEM4 begins to diverge below the observed wind speed whereas FASTEM5 diverges above more severely. The MW model gives a slight low bias of as much as 1 m s^{-1} at $10\text{-}15 \text{ m s}^{-1}$ but recovers to near zero at higher speeds. The overall root-mean-squared error in clear conditions for the MW model is 1.3 m s^{-1} (equivalent to WindSat) and, because of its low bias over the range of observed wind speeds, is chosen to generate the DPR GMFs.

The DPR GMF was generated by averaging the observed σ_0 from the DPR Level 2 product (Iguchi and Meneghini 2014), removing the two-way attenuation from gases and cloud liquid water (which are determined from the GMI retrievals), in wind speed bins with 0.5 m s^{-1} spacing from 0 to 10 m s^{-1} , 1 m s^{-1} spacing between 10 and 20 m s^{-1} , and 2 m s^{-1} spacing above 20 m s^{-1} . Note that all of the results presented in this manuscript are from observations taken between 25 August 2014 (when the most recent phase shift code for DPR was implemented) and 30 April

2015. Earlier observations used different phase shift codes and attenuator settings, which had some slight impact on the GMFs (not shown). The standard deviation in each bin is also calculated as is the correlation coefficient in the case of the matched KuPR-KaPR beams. The standard deviation serves as an implicit indicator of the quality of the derived GMF: Low values are desirable because they indicate that the 10m wind speed retrieved by GMI is sufficient to represent the sea state for the purposes of reproducing σ_0 , and, when used in the combined framework, provide a stronger constraint on the PIA contributed by the precipitation column. The theoretical minimum standard deviation of σ_0 for DPR, assuming the signal-to-noise ratio is large (true under almost all non-rain conditions), depends on the number of independent samples, N , taken. If the surface is modeled as a Rayleigh target (an incoherent sum from many specular points on the surface without any dominant scattering contribution) and a logarithmic receiver is used, then the standard deviation in dB is given by (Sauvageot 1992):

$$std(\sigma_0) = \frac{5.57}{\sqrt{N}}, \quad (3)$$

where N depends on incidence angle and varies between 100 and about 110 . Using these numbers, the nominal standard deviation in σ_0 , from sampling alone, is a bit more than 0.5 dB.² Values higher than 0.5 dB could be caused by random errors in the GMI wind reference (this is compounded when the sensitivity of σ_0 to wind is high) or that something other than wind speed is contributing the variation of σ_0 , resulting in diminished impact of the σ_0 observation on the precipitation retrieval. In Figure 3, the standard deviation of σ_0 for the KuPR, in normal scan (NS) mode, and KaPR, in matched-scan (MS) and high-sensitivity (HS) modes, is shown as a function of DPR incidence angle for three wind speed bins centered on 0.5 m s^{-1} , 5 m s^{-1} , and 15 m s^{-1} .

²For off-nadir incidence, where there are multiple samples from the surface, a case can be made for integrating over all the data from the surface.

This should reduce the standard deviation of the σ_0 ; however, in the DPR processing, the σ_0 is based on the peak return power, not the integrated power.

At the low wind speed, the standard deviation is quite high (nearly 10 dB), particularly off nadir, but smaller (still 2-4 dB) near nadir at both frequencies (the lower Ku values are likely due to the saturation of the KuPR receiver). As the wind becomes calm, the surface is nearly specular and the sensitivity to small changes in wind speed is quite high off nadir, so random error in the reference wind is thought to primarily contribute to the large standard deviation there. Long-period swell also provides an increasing contribution to variation in σ_0 (Tran et al. 2007) that is unrelated to the local wind speed. Finally, since the change in σ_0 with respect to incidence angle is also high at low wind speeds, small changes in the incidence angle (the standard deviation of DPR incidence angle was around 0.01° in each angle bin) may also contribute to the high standard deviation at off-nadir angles.

At moderate and high wind speeds, the standard deviations are much lower and the pattern is shifted slightly to relatively high values near nadir and at the largest off-nadir angles, with minima around 9° for KuPR. Specular effects can again explain the near-nadir maximum, whereas the off-nadir maxima are likely a result of wind direction sensitivity (Wentz et al. 1984). The KaPR standard deviations are slightly higher for the MS than the HS data due to the shorter pulse width, and are qualitatively similar to the KuPR data. The effect of more stringent quality control (reduction of the cloud LWP, its spatial variability, and cost function thresholds by 50%; denoted QC2 in Figure 3) is also most evident here in reducing the KaPR standard deviation, but the differences are negligible enough (0.01 dB) that the original thresholds (QC1) are used to generate databases for the combined algorithm as this choice of thresholds provides more data, especially at higher wind speeds.

263 The two-dimensional GMFs of σ_0 are shown in Figure 4. Most of the variability is exhibited
 264 at low wind speeds at both Ku and Ka bands³. However, σ_0 continues to decrease near nadir for
 265 wind speeds as high as 30 m s^{-1} , which is approximately the upper limit of the reliable data that
 266 has been collected so far. Off-nadir, σ_0 appears to reach maxima at increasing wind speeds with
 267 incidence angle. The standard deviation of σ_0 reaches minima near the 0.5 dB sampling limit
 268 at $5\text{-}15^\circ$ and wind speeds between 5 and 10 m s^{-1} . There is also a minimum in the standard
 269 deviation at Ku band (but not Ka band) at very low wind speeds near nadir. This is an artifact of
 270 the saturation of the Ku receiver when $\sigma_0 \geq 22.5 \text{ dB}$ (The Ka receiver saturates closer to 40 dB,
 271 which is only observed over some land and ice surfaces). The higher standard deviations at the
 272 off-nadir angles are likely a result of wind-direction induced variability in σ_0 . In Figure 4f the
 273 observed Ku-band σ_0 is compared to the cutoff-invariant two-scale model (Soriano and Guérin
 274 2008) using the Durden-Vesecky single-amplitude wave spectra (Durden and Vesecky 1985). This
 275 model appears to produce a flatter σ_0 when viewed with respect to incidence angle at low wind
 276 speeds, but at winds above about 8 m s^{-1} has a comparable shape to the observed GMF minus a
 277 small (1 dB) offset. These results are consistent with the comparisons of this model to airborne
 278 observations of σ_0 reported by Majurec et al. (2014).

279 The Ku-Ka σ_0 correlation (Figure 4e) is an important component of the dual-frequency sur-
 280 face reference technique (DSRT; Meneghini et al. (2012)). In the DSRT, σ_0 is replaced by the
 281 differential σ_0 :

$$\delta\sigma_0 = \sigma_0(Ka) - \sigma_0(Ku) \quad (4)$$

282 and the method provides an estimate of the differential PIA, $A(Ka)\text{-}A(Ku)$. The errors in both
 283 single-frequency SRT and DSRT methods are dominated by the fluctuations in the rain-free ref-

³the Ka HS GMF is not shown, but is essentially identical to the MS data with a -0.2 dB offset owing to the inability of the larger pulse width
 to capture the surface peak as effectively, especially near nadir.

284 erence data: σ_0 and $\delta\sigma_0$. As the correlation between $\sigma_0(\text{Ku})$ and $\sigma_0(\text{Ka})$ increases, the variance
 285 in $\delta\sigma_0$ decreases so that the DSRT provides a potentially more accurate estimate of the path at-
 286 tenuations. The correlations, which are near 0.8 in most DPR angle bins when all wind speeds
 287 are considered, reduce to 0.1-0.4 for most wind speeds $> 5 \text{ m s}^{-1}$ and off-nadir incidence angles.
 288 This suggests that wind is responsible for most of the covariance in Ku and Ka σ_0 but near-nadir
 289 and at low winds the stronger correlations make the DSRT technique particularly useful.

290 **3. Combined Radar-Radiometer Retrieval of Precipitation and Surface Wind**

291 The MW emissivity model (optimized for GMI) and DPR wind- σ_0 GMFs described in section
 292 2 are implemented in the forward modeling component of the GPM Combined Radar Radiometer
 293 (CORRA) retrieval algorithm. A description of the radar component of this algorithm is given by
 294 Grecu et al. (2011) and a more complete description of the algorithm architecture can be found in
 295 the Algorithm Theoretical Basis Document (Olson and Masunaga 2015); for the purposes of this
 296 manuscript, a brief summary and example case are presented in this section followed by validation
 297 statistics. It is difficult to directly ascertain the improvement (if any) in rainfall estimates over
 298 ocean owing to the lack of reliable direct measurements, but the algorithm can be assessed as to
 299 how well the forward model matches GPM observations and buoy observations of wind speed.
 300 The impact on retrieved precipitation amounts is also shown in this section.

301 *a. Algorithm Description*

302 The CORRA algorithm uses an ensemble filter technique (Evensen 2006) to retrieve a set of pre-
 303 cipitation profiles that are consistent with observations from KuPR, GMI, and KaPR (where avail-
 304 able). The first step in this process is the creation of an ensemble of solutions that fit the observed
 305 KuPR reflectivity profile without any consideration of the GMI, KaPR, or KuPR σ_0 observations.

306 The randomly perturbed properties of each profile solution include the vertical profile of the hy-
 307 drometer particle size distribution (PSD) intercept parameter (N_w), degree of non-uniform beam
 308 filling, the cloud liquid water profile, relative humidity, and 10m wind speed. For each solution,
 309 the associated Ku and Ka σ_0 , Ka reflectivities, and GMI radiances are calculated. The calculation
 310 of Ka reflectivity's accounts for multiple scattering enhancements using the multiscatter library
 311 developed by Hogan and Battaglia (2008).

312 The ensemble is then filtered using the observed Ku σ_0 , GMI radiances, and Ka reflectivities and
 313 σ_0 (where available). This is done by constructing an $n_{var} \times n_{memb}$ vector \mathbf{X}_{ens} representing the
 314 ensemble variables to be updated, including the perturbed variables, e.g., N_w and 10m wind, and
 315 derived/forward modeled variables, e.g., precipitation rate and brightness temperature. A separate
 316 $n_{obs} \times n_{memb}$ vector \mathbf{Y}_{ens} consists of the forward modeled variables corresponding to the $n_{obs} \times 1$
 317 observation vector \mathbf{Y}_{obs} (\mathbf{R} is the corresponding observation error), which contains the observed
 318 σ_0 , brightness temperatures, and Ka reflectivities. The ensemble state vector \mathbf{X}_{ens} is then updated
 319 using the sample covariance:

$$\mathbf{X}_{ens} = \mathbf{X}_{ens} + \mathbf{Cov}_{XY}(\mathbf{Cov}_{YY} + \mathbf{R})^{-1}(\mathbf{Y}_{obs} - \mathbf{Y}_{ens}). \quad (5)$$

320 The algorithm output is derived from the updated ensemble and includes both mean and standard
 321 deviations of the geophysical parameters of the ensemble and forward modeled observations. This
 322 update is done separately for the Ku-only full swath (denoted as NS in GPM products) and Ku+Ka
 323 inner swath (MS products).

324 *b. Example Case*

325 To illustrate the update process described by Eq. 5, the retrieval algorithm is applied to a GPM
 326 overpass of a developing cyclone off the eastern coast of the United State on 26 January 2015 (Fig-

ure 5). This case provides an opportunity to examine the algorithm under a variety of precipitation and surface wind conditions.

The correlations (calculated from the initial, unfiltered ensemble) between the each observation type and the surface rain rate, as well as the correlations between each observation type and the 10m wind speed, are shown in Figure 6 for both radar frequencies and the horizontally-polarized GMI channels from 10-36 GHz (which are most sensitive to rain and wind over water surfaces). It is evident from these sensitivities that algorithm adjustments to precipitation rate in convective rain (echoes greater than 40 dBZ; purple colors in Figure 5) are mostly a response to the initial Ku and Ka σ_0 error, whereas adjustments in stratiform rain are mostly a response to the Ka σ_0 and GMI Tbs (note that in the heaviest rain, the correlation between rain rate and 36H Tb becomes negative as scattering dominates over emission). Note that in extremely heavy precipitation with large amounts of ice aloft, the variability of Ka σ_0 due to multiple scattering begins to overwhelm the attenuation, and the correlation decreases. In these cases, the algorithm relies mostly on Ku σ_0 to adjust the initial ensemble rain rates. In light and moderate rainfall, the 10m wind adjustment is mostly a response to Ku σ_0 , especially away from the approximately 9° incidence angle at which Ku σ_0 is insensitive to wind. Nevertheless there is some sensitivity of the 10 and 19 GHz radiances and Ka σ_0 to wind under lighter precipitation. Due to the finite number of ensemble members, there are some spurious negative correlations between wind and the Tbs in heavier rain, but these are weak and do not substantially impact the output. The degree to which the ensemble spread is reduced after the filtering step is indicative of the overall information content in the observations for each variable of interest, and is provided as part of the standard CORRA output.

348 *c. Internal Validation*

349 Output from 400 GPM orbits between September 2014 and January 2015 are analyzed to assess
350 the internal consistency between the forward model and observations before and after filtering.
351 The mean bias and root-mean-square (rms) error between the initial ensemble mean and filtered
352 ensemble mean for both NS (Ku+GMI) and MS (Ku+Ka+GMI) are given in Table 2. There is a
353 general cold bias to the initial simulated brightness temperatures (Tbs) at all frequencies (although
354 a warm bias is present in the 18 and 36 GHz channels at rain rates exceeding 10 mm hr⁻¹). Both
355 the rms error and magnitude of the bias are reduced after filtering as expected. The MS error and
356 bias are larger than the NS error and bias because the initial ensemble profiles are constrained by
357 the additional Ka band information and are less free to be adjusted to match the GMI radiances.
358 In other words, the NS retrievals are over-fit to the Tbs, which suggests an increase in their error
359 values in **R** is warranted.

360 The initial and filtered rms error and bias of σ_0 is shown as a function of scan angle in Figure 7.
361 There is a significant reduction in Ku rms error at all scan angles. The Ka error values are higher
362 due to the stronger attenuation and multiple scattering effects, but errors are still reduced by nearly
363 50% after the filtering step. The bias plots show a pattern of initial errors that are consistent with
364 a low bias in the ENV wind (too high near nadir and too low off nadir). This bias appears to be
365 more significant than any systematic bias in the precipitation attenuation, which would have the
366 same sign regardless of scan angle.

367 *d. External Validation*

368 During September 2014-January 2015, 606 buoy observations from the ICOADS database were
369 identified as being within 30 minutes of a GPM overpass and in the KuPR swath (308 of these

370 were within the KaPR swath) at the same time that DPR detected precipitation in the pixel nearest
371 to the buoy location. These observations were used to validate the CORRA wind retrieval.

372 The wind rmse and bias are shown in Figure 8. Similar to the MERRA data analyzed in section
373 2, these background winds are biased high below 3 m s^{-1} and biased low at higher wind speeds
374 relative to the buoy observations. Root-mean-square errors increase from 2 m s^{-1} to 4 m s^{-1}
375 and NS errors are slightly higher than the MS or ENV errors. However, the bias is significantly
376 reduced in the filtered datasets relative to the initial winds, indicating that while the retrievals are
377 noisy, adjustments tend to be in the correct direction (this is consistent with the initial and filtered
378 T_b and σ_0 biases as well).

379 The wind error is shown as a function of incidence angle in Figure 9. It is evident that the
380 largest errors occur near the 9° incidence angle where there is little sensitivity of σ_0 to wind
381 speed (Figures 4 and 6 illustrate this behavior). Near nadir and beyond 12° incidence angles, the
382 sensitivity is stronger and the wind errors are much smaller. The NS errors are similar and the
383 MS errors are smaller than the 4.26 m/s error of ASCAT under raining conditions (Portabella et al.
384 2012) and 3.5 m/s error Quikscat retrievals using a neural network to compensate for rain effects
385 (Stiles and Dunbar 2010). These are also within the range of 2 to 5 m/s accuracy (depending on
386 rain rate) of a globally-applicable rainy-atmosphere WindSat wind retrieval algorithm (Meissner
387 and Wentz 2009). When stratified by rainfall rate, wind speed errors are similar for light (< 1
388 mm hr^{-1}) and moderate ($1 \text{ mm hr}^{-1} < R < 10 \text{ mm hr}^{-1}$) precipitation rates, but increase at
389 heavier precipitation rates as the wind-induced variability in σ_0 and brightness temperatures is
390 overwhelmed by the precipitation effects.

391 *e. Impact on Precipitation Retrieval*

392 Although the retrieval of wind in precipitation is useful for many applications, one of the main
393 purposes of this work is to improve the precipitation retrieval by enforcing an internal consis-
394 tency between the surface emissivity (which depends on wind) and observed σ_0 which depends
395 on both wind and precipitation-induced path-integrated attenuation (PIA). In this section we show
396 the impact of switching from the SRT PIA (which infers PIA by comparing the observed σ_0 to a
397 reference outside the precipitation) to the coupled σ_0 -emissivity model.

398 Theoretically, the use of σ_0 as an observation (instead of SRT-derived PIA) should impact the
399 agreement between observed and modeled Tbs in two ways: First, through adjustments to the rain
400 column to match the observed σ_0 by changing the PIA, and second, via changes in the surface
401 emissivity. The relative importance of these mechanisms depends on the relative sensitivity of
402 the Tbs and σ_0 to changes in the rain column and surface wind. Figure 10 shows the change
403 in near-surface precipitation rate retrieved by the GPM combined algorithm over ocean surfaces
404 equatorward of 55° latitude (to eliminate possible sea ice) when the SRT PIA (single frequency for
405 NS retrievals in top panels; DSRT in the MS retrieval shown in the bottom panels) is replaced with
406 the observed σ_0 in the observation vector. Light precipitation ($< 1 \text{ mm hr}^{-1}$) is increased slightly
407 in the NS swath, predominantly at wind speeds $> 10 \text{ m s}^{-1}$ and at incidence angles less than 12° .
408 The discontinuities in the $10\text{-}12^\circ$ range are an artifact of the unavailability of the low-frequency
409 GMI channels near the edge of the DPR swath (the deconvolution procedure requires coverage
410 of the full footprint within the DPR swath). This suggests that GMI Tbs are driving the increase
411 in precipitation, which is consistent with the weak Ku σ_0 -precipitation correlation in light rain
412 (Figure 6). Near the edges of the DPR swath, where the GMI Tbs are not used, there is not enough

413 information to significantly adjust the precipitation rate because the Ku-band PIA is small relative
414 to the uncertainty in σ_0 , so the SRT and coupled method have the same information content.

415 At moderate ($1 \text{ mm hr}^{-1} < R < 10 \text{ mm hr}^{-1}$) precipitation rates, the wind- σ_0 correlation is
416 still larger than the rain correlation at Ku band whereas Tbs are more sensitive to the precipitation
417 (although there is still some wind sensitivity especially at 10H). This results in some compensating
418 behavior, where it is “easier” for the algorithm to increase the wind speed to satisfy the Ku σ_0
419 observation but must reduce the precipitation rate to be consistent with the Tbs. In heavy rain ($>$
420 10 mm hr^{-1}), the ensemble variance in σ_0 and the Tbs is dominated by variance in the rain column,
421 rather than surface wind, and where both observations are available only a very small reduction
422 in precipitation is noted with the coupled forward model relative to the SRT method. When only
423 Ku σ_0 is available in the outer swath, however, there is a reduction in precipitation relative to the
424 SRT version. The mean precipitation rate from the coupled model is more consistent across the
425 different scan angles than the SRT version (not shown) which suggests that the SRT PIA may be
426 biased high at the off-nadir angles and wind speeds from $5\text{-}10 \text{ m s}^{-1}$.

427 The Ku-Ka (MS) retrievals are generally more stable when comparing the SRT and coupled
428 versions of the algorithm, but some changes are still notable. The increase in light precipitation
429 is still present, but moderate and heavy precipitation show some different behavior from the NS
430 retrievals with increases in light winds (below about 5 m s^{-1}) and little change at higher wind
431 speeds. There is not much sensitivity of Tb to wind at low wind speeds, so this appears to be
432 driven by an increase in the inferred PIA in the coupled model relative to the dual-frequency SRT.

433 **4. Summary**

434 The Global Precipitation Measurement core satellite launched in February, 2014 carries a passive
435 microwave imager (GMI) and dual-frequency radar (DPR) designed specifically to provide the

most accurate instantaneous precipitation estimates currently available from space and serve as a reference for precipitation retrievals from other passive microwave imagers with similar channel sets (Kummerow et al. 2015). The GPM combined algorithm plays a key role in this process by providing precipitation estimates that are consistent with both GMI and DPR measurements. This algorithm uses physically-based forward models to simulate GMI and DPR measurements and it is desirable that those models use the same geophysical input parameters wherever possible.

This study explored the feasibility of using internally consistent relationships between wind, emissivity, and backscatter for water surfaces in the combined algorithm. We first evaluated the FASTEM 4/5 (Liu et al. 2011) and Meissner and Wentz (2012) emissivity models in a GMI-only non-precipitation retrieval against buoy observations obtained from the ICOADS dataset. The Meissner-Wentz model provided the lowest root-mean-square error (1.3 m s^{-1}) and was used to create a geophysical model function (GMF) for DPR Ku and Ka σ_0 as a function of 10m wind speed and incidence angle by matching the GMI retrievals to DPR observations under clear conditions.

The Meissner-Wentz emissivity model and DPR GMFs were then implemented in the GPM combined algorithm. This coupled forward model indicated that the sensitivity of σ_0 to wind at Ku band dominates the precipitation sensitivity particularly in light to moderate rain and at low wind speeds, where the brightness temperatures are more sensitive to precipitation (although there is still some wind sensitivity, particularly at 10 and 18 GHz at horizontal polarization in light and shallow precipitation). Therefore, the surface reference (SRT) estimate of the DPR path-integrated attenuation (PIA) was replaced with σ_0 in the observation vector. This is desirable because σ_0 is directly observed by DPR while the SRT PIA includes implicit assumptions and can be unphysically negative in light rain. Because σ_0 depends on both the 10m wind speed and

attenuation from atmospheric gases, clouds, and precipitation, the 10m wind speed was added to the retrieval state vector.

The combined wind/precipitation retrievals were then evaluated against the ICOADS buoy dataset under precipitating conditions, which have been a challenge for surface wind retrievals from standalone passive radiometers (e.g., WindSat) or scatterometers. Although the retrievals were noisier than under clear conditions (rmse of 3.7 m s^{-1} for Ku+GMI and 3.2 m s^{-1} for Ku+Ka+GMI), there was a significant reduction in the bias from the background data provided by GANAL (-10%) to the Ku+GMI (-3%) and Ku+Ka+GMI (-5%) retrievals. The impact on precipitation retrievals was also evaluated. Ku+GMI retrievals of precipitation increased slightly on the light end ($< 1 \text{ mm hr}^{-1}$) and decreased in moderate to heavy precipitation ($> 1 \text{ mm hr}^{-1}$) due to compensating effects of wind on σ_0 and emissivity requiring changes in the precipitation column to maintain consistency with the observations. The Ku+Ka+GMI retrievals, being additionally constrained by the Ka reflectivity, did not change as much although a slight increase in moderate and heavy precipitation at low wind speeds was noted.

While GPM was not designed specifically to measure ocean surface winds, this study demonstrates that such measurements are quite feasible in clear-sky conditions. In precipitation, using a coupled emissivity-backscatter GMF produces reasonable results that achieve the goal of internal consistency in the combined algorithm. The results presented here should only be considered as a proof of concept, as additional details that we did not consider, such as wind direction, the effect of rain on the scattering properties of water surfaces, and spatial correlation of the wind field, are left to future work.

Acknowledgments. This work was supported under NASA Cooperative Agreement NNX12AD03A and Precipitation Measurement Missions Program Scientist Dr. Ramesh

482 Kakar. We would also like to thank Dr. Thomas Meissner of Remote Sensing Systems for
483 providing the computational codes for the Meissner-Wentz emissivity model, and Dr. Simone
484 Tanelli of NASA JPL/CalTech for providing the cutoff-invariant two-scale Durden-Vesecky
485 model data. Finally, we would like to thank the three anonymous reviewers whose comments and
486 suggestions greatly improved the quality of this manuscript.

487 **References**

- 488 Albrecht, B. A., C. W. Fairall, D. W. Thomson, A. B. White, J. B. Snider, and W. H. Schu-
489 bert, 1990: Surface-based remote sensing of the observed and the adiabatic liquid water
490 content of stratocumulus clouds. *Geophysical Research Letters*, **17** (1), 89–92, doi:10.1029/
491 GL017i001p00089, URL <http://dx.doi.org/10.1029/GL017i001p00089>.
- 492 Battaglia, A., and C. Simmer, 2008: How does multiple scattering affect the spaceborne W-Band
493 radar measurements at ranges close to and crossing the sea-surface range? *Geoscience and*
494 *Remote Sensing, IEEE Transactions on*, **46** (6), 1644–1651, doi:10.1109/TGRS.2008.916085.
- 495 Boukabara, S.-A., and Coauthors, 2011: MiRS: An All-Weather 1DVAR satellite data assimilation
496 and retrieval system. *Geoscience and Remote Sensing, IEEE Transactions on*, **49** (9), 3249–
497 3272, doi:10.1109/TGRS.2011.2158438.
- 498 Donnelly, W. J., J. R. Carswell, R. E. McIntosh, P. S. Chang, J. Wilkerson, F. Marks, and P. G.
499 Black, 1999: Revised ocean backscatter models at C and Ku band under high-wind con-
500 ditions. *Journal of Geophysical Research: Oceans*, **104** (C5), 11 485–11 497, doi:10.1029/
501 1998JC900030, URL <http://dx.doi.org/10.1029/1998JC900030>.
- 502 Draper, D., D. Newell, F. Wentz, S. Krimchansky, and G. Skofronick-Jackson, 2015: The global
503 precipitation measurement (GPM) microwave imager (GMI): Instrument overview and early on-

orbit performance. *IEEE Journal of Selected Topics in Applied Earth Observations and Remote Sensing*, in review.

Durden, S., and J. Vesecky, 1985: A physical radar cross-section model for a wind-driven sea with swell. *Oceanic Engineering, IEEE Journal of*, **10** (4), 445–451, doi:10.1109/JOE.1985.1145133.

Elsaesser, G. S., and C. D. Kummerow, 2008: Toward a fully parametric retrieval of the nonraining parameters over the global oceans. *J. Appl. Meteor. Climatol.*, **47**, 1599–1618.

Evensen, G., 2006: *Data Assimilation: The Ensemble Kalman Filter*. Springer, 280 pp.

Fernandez, D. E., J. R. Carswell, S. Frasier, P. S. Chang, P. G. Black, and F. D. Marks, 2006: Dual-polarized C- and Ku-band ocean backscatter response to hurricane-force winds. *Journal of Geophysical Research: Oceans*, **111** (C8), n/a–n/a, doi:10.1029/2005JC003048, URL <http://dx.doi.org/10.1029/2005JC003048>.

Freilich, M. H., and B. A. Vanhoff, 2003: The relationship between winds, surface roughness, and radar backscatter at low incidence angles from TRMM Precipitation Radar measurements. *J. Atmos. Oceanic Technol.*, **20**, 549–562.

GPM Science Team, 2015: GPM Level 1C R Common Calibrated Brightness Temperatures Collocated, version 04. NASA Goddard Earth Science Data and Information Services Center (GES DISC), Greenbelt, MD, USA, URL http://disc.sci.gsfc.nasa.gov/datacollection/GPM_1CGPMGMI_R_V04.html, accessed 16 May 2015.

Grecu, M., W. S. Olson, and E. N. Anagnostou, 2004: Retrieval of precipitation profiles from multiresolution, multifrequency active and passive microwave observations. *J. Appl. Meteor.*, **43**, 562–575.

526 Grecu, M., L. Tian, W. S. Olson, and S. Tanelli, 2011: A robust dual-frequency radar profiling
527 algorithm. *J. Appl. Meteor. Climatol.*, **50**, 1543–1557.

528 Haddad, Z. S., E. A. Smith, C. D. Kummerow, T. Iguchi, M. R. Farrar, S. L. Durden, M. Alves, and
529 W. S. Olson, 1997: The TRMM ‘Day-1’ radar/radiometer combined rain-profiling algorithm. *J.*
530 *Meteor. Soc. Japan*, **75**, 799–809.

531 Hogan, R. J., and A. Battaglia, 2008: Fast lidar and radar multiple-scattering models: Part 2:
532 Wide-angle scattering using the time-dependent two-stream approximation. *J. Atmos. Sci.*, **65**,
533 3636–3651.

534 Hou, A. Y., and Coauthors, 2014: The Global Precipitation Measurement Mission. *Bull. Amer.*
535 *Meteor. Soc.*, **95**, 701–722.

536 Hsu, S. A., E. A. Meindl, and D. B. Gilhousen, 1994: Determining the power-law wind-profile
537 exponent under near-neutral stability conditions at sea. *J. Appl. Meteor.*, **33**, 757–765.

538 Iguchi, T., T. Kozu, J. Kwiatkowski, , R. Meneghini, J. Awaka, and K. Okamoto, 2009: Uncertain-
539 ties in the rain profiling algorithm for the TRMM Precipitation Radar. *J. Meteor. Soc. Japan*,
540 **87A**, 1–30.

541 Iguchi, T., T. Kozu, R. Meneghini, J. Awaka, and K. Okamoto, 2000: Rain-profiling algorithm for
542 the TRMM Precipitation Radar. *J. Appl. Meteor.*, **39**, 2038–2052.

543 Iguchi, T., and R. Meneghini, 2014: GPM DPR Level 2A DPR Environment V03 (GPM
544 2ADPR), version 03. NASA Goddard Earth Science Data and Information Services Cen-
545 ter (GES DISC), Greenbelt, MD, USA, URL [http://disc.sci.gsfc.nasa.gov/datacollection/GPM_](http://disc.sci.gsfc.nasa.gov/datacollection/GPM_2ADPR_V03.html)
546 [2ADPR_V03.html](http://disc.sci.gsfc.nasa.gov/datacollection/GPM_2ADPR_V03.html), accessed 8 April 2015.

547 Kummerow, C. D., D. Randel, M. Kulie, N.-Y. Wang, R. Ferraro, S. J. Munchak, and V. Petkovic,
548 2015: The evolution of the Goddard Profiling Algorithm to a fully parametric scheme. *J. Atmos.*
549 *Oceanic Technol.*, accepted.

550 Li, L., E. Im, L. Connor, and P. Chang, 2004: Retrieving ocean surface wind speed from the
551 TRMM Precipitation Radar measurements. *Geoscience and Remote Sensing, IEEE Transac-*
552 *tions on*, **42** (6), 1271–1282, doi:10.1109/TGRS.2004.828924.

553 Li, L., E. Im, S. L. Durden, and Z. S. Haddad, 2002: A surface wind model-based method to
554 estimate rain-induced radar path attenuation over ocean. *J. Atmos. Oceanic Technol.*, **19**, 658–
555 672.

556 Liebe, H., G. Hufford, and T. Manabe, 1991: A model for the complex permittivity of water
557 at frequencies below 1 THz. *International Journal of Infrared and Millimeter Waves*, **12** (7),
558 659–675, doi:10.1007/BF01008897, URL <http://dx.doi.org/10.1007/BF01008897>.

559 Liu, Q., F. Weng, and S. English, 2011: An improved fast microwave water emissivity model. *Geo-*
560 *science and Remote Sensing, IEEE Transactions on*, **49** (4), 1238–1250, doi:10.1109/TGRS.
561 2010.2064779.

562 Majurec, N., J. Johnson, S. Tanelli, and S. Durden, 2014: Comparison of model predictions with
563 measurements of Ku- and Ka-band near-nadir normalized radar cross sections of the sea sur-
564 face from the Genesis and Rapid Intensification Processes experiment. *Geoscience and Remote*
565 *Sensing, IEEE Transactions on*, **52** (9), 5320–5332, doi:10.1109/TGRS.2013.2288105.

566 Meissner, T., and F. Wentz, 2009: Wind-vector retrievals under rain with passive satellite mi-
567 crowave radiometers. *Geoscience and Remote Sensing, IEEE Transactions on*, **47** (9), 3065–
568 3083.

569 Meissner, T., and F. Wentz, 2012: The emissivity of the ocean surface between 6 and 90 GHz over
570 a large range of wind speeds and earth incidence angles. *Geoscience and Remote Sensing, IEEE*
571 *Transactions on*, **50 (8)**, 3004–3026, doi:10.1109/TGRS.2011.2179662.

572 Meneghini, R., T. Iguchi, T. Kozu, L. Liao, K. Okamoto, J. A. Jones, and J. Kwiatkowski, 2000:
573 Use of the surface reference technique for path attenuation estimates from the TRMM Precipi-
574 tation Radar. *J. Appl. Meteor.*, **39**, 2053–2070.

575 Meneghini, R., J. A. Jones, T. Iguchi, K. Okamoto, and J. Kwiatkowski, 2004: A hybrid surface
576 reference technique and its application to the TRMM Precipitation Radar. *J. Atmos. Oceanic*
577 *Technol.*, **21**, 1645–1658.

578 Meneghini, R., L. Liao, S. Tanelli, and S. Durden, 2012: Assessment of the performance of a
579 dual-frequency surface reference technique over ocean. *Geoscience and Remote Sensing, IEEE*
580 *Transactions on*, **50 (8)**, 2968–2977, doi:10.1109/TGRS.2011.2180727.

581 Migliaccio, M., and A. Reppucci, 2006: A review of sea wind vector retrievals by means of
582 microwave remote sensing. *Proceedings of the European Microwave Association Vol*, **136**, 140.

583 Mitrescu, C., T. L’Ecuyer, J. Haynes, S. Miller, and J. Turk, 2010: Cloudsat precipitation profiling
584 algorithm – model description. *J. Appl. Meteor. Climatol.*, **49**, 991–1003.

585 Munchak, S. J., and C. D. Kummerow, 2011: A modular optimal estimation method for combined
586 radar-radiometer precipitation profiling. *J. Appl. Meteor. Climatol.*, **50**, 433–448.

587 NASA/GMAO, 2008: MERRA Reanalysis Data. NASA Goddard Earth Science Data and Infor-
588 mation Services Center (GES DISC), Greenbelt, MD, USA, URL [http://disc.sci.gsfc.nasa.gov/](http://disc.sci.gsfc.nasa.gov/mdisc)
589 mdisc, accessed 27 February 2015.

590 NCDC/NESDIS/NOAA, 2011, updated monthly: International Comprehensive Ocean-
 591 Atmosphere Data Set Release 2.5, Individual Observations. NOAA NCDC, Asheville, NC,
 592 USA, URL <http://www1.ncdc.noaa.gov/pub/data/icoads2.5/>, accessed 8 May 2015.

593 Negri, A. J., R. F. Adler, and C. D. Kummerow, 1989: False-color display of Special Sensor
 594 Microwave/Imager (SSM/I) data. *Bull. Amer. Meteor. Soc.*, **70**, 146–151.

595 O’Dell, C. W., F. J. Wentz, and R. Bennartz, 2008: Cloud liquid water path from satellite-based
 596 passive microwave observations: A new climatology over the global oceans. *J. Climate*, **21**,
 597 1721–1739.

598 Olson, W. S., and H. Masunaga, 2015: GPM Combined Radar - Radiometer Precipitation Al-
 599 gorithm Theoretical Basis Document (Version 3). NASA ATBD, NASA GSFC, 59 pp. URL
 600 http://pps.gsfc.nasa.gov/Documents/Combined_algorithm_ATBD.2014.restore16-1.pdf.

601 Portabella, M., A. Stoffelen, W. Lin, A. Turiel, A. Verhoef, J. Verspeek, and J. Ballabrera-Poy,
 602 2012: Rain effects on ascat-retrieved winds: Toward an improved quality control. *Geoscience*
 603 *and Remote Sensing, IEEE Trans. Geosci. Rem.*, **50** (7), 2495–2506.

604 Quilfen, Y., C. Prigent, B. Chapron, A. A. Mouche, and N. Houti, 2007: The potential of
 605 QuikSCAT and WindSat observations for the estimation of sea surface wind vector under se-
 606 vere weather conditions. *Journal of Geophysical Research: Oceans*, **112** (C9), n/a–n/a, doi:
 607 10.1029/2007JC004163, URL <http://dx.doi.org/10.1029/2007JC004163>.

608 Rapp, A. D., M. Lebsock, and C. Kummerow, 2009: On the consequences of resampling mi-
 609 crowave radiometer observations for use in retrieval algorithms. *J. Appl. Meteor. Climatol.*, **48**,
 610 1981–1993.

611 Rienecker, M. M., and Coauthors, 2011: MERRA: NASA's modern-era retrospective analysis for
 612 research and applications. *J. Climate*, **24**, 3624–3648.

613 Rosenkranz, P. W., 1998: Water vapor microwave continuum absorption: A comparison of
 614 measurements and models. *Radio Science*, **33** (4), 919–928, doi:10.1029/98RS01182, URL
 615 <http://dx.doi.org/10.1029/98RS01182>.

616 Sauvageot, H., 1992: *Radar meteorology*. Artech House Publishers.

617 Seto, S., and T. Iguchi, 2007: Rainfall-induced changes in actual surface backscattering cross
 618 sections and effects on rain-rate estimates by spaceborne precipitation radar. *J. Atmos. Oceanic
 619 Technol.*, **24**, 1693–1709.

620 Soriano, G., and C.-A. Guérin, 2008: A cutoff invariant two-scale model in electromagnetic scat-
 621 tering from sea surfaces. *Geoscience and Remote Sensing Letters, IEEE*, **5** (2), 199–203.

622 Stiles, B., and R. Dunbar, 2010: A neural network technique for improving the accuracy of scat-
 623 terometer winds in rainy conditions. *Geoscience and Remote Sensing, IEEE Transactions on*,
 624 **48** (8), 3114–3122.

625 Stiles, B., and S. Yueh, 2002: Impact of rain on spaceborne Ku-band wind scatterometer data. *Geo-
 626 science and Remote Sensing, IEEE Transactions on*, **40** (9), 1973–1983, doi:10.1109/TGRS.
 627 2002.803846.

628 Tran, N., B. Chapron, and D. Vandemark, 2007: Effect of long waves on Ku-band ocean radar
 629 backscatter at low incidence angles using TRMM and altimeter data. *Geoscience and Remote
 630 Sensing Letters, IEEE*, **4** (4), 542–546, doi:10.1109/LGRS.2007.896329.

631 Tretyakov, M., V. Parshin, M. Koshelev, V. Shanin, S. Myasnikova, and A. Krupnov, 2003:
 632 Studies of 183 GHz water line: Broadening and shifting by air, N₂ and O₂ and integral in-

633 tensity measurements. *Journal of Molecular Spectroscopy*, **218** (2), 239 – 245, doi:http://dx.
634 doi.org/10.1016/S0022-2852(02)00084-X, URL [http://www.sciencedirect.com/science/article/
635 pii/S002228520200084X](http://www.sciencedirect.com/science/article/pii/S002228520200084X).

636 Uhlhorn, E. W., P. G. Black, J. L. Franklin, M. Goodberlet, J. Carswell, and A. S. Goldstein,
637 2007: Hurricane surface wind measurements from an operational stepped frequency microwave
638 radiometer. *Mon. Wea. Rev.*, **135**, 3070–3085.

639 Weissman, D. E., B. W. Stiles, S. M. Hristova-Veleva, D. G. Long, D. K. Smith, K. A. Hilburn,
640 and W. L. Jones, 2012: Challenges to satellite sensors of ocean winds: Addressing precipitation
641 effects. *J. Atmos. Oceanic Technol.*, **29**, 356–374.

642 Wentz, F. J., S. Peteherych, and L. A. Thomas, 1984: A model function for ocean radar cross
643 sections at 14.6 GHz. *Journal of Geophysical Research: Oceans*, **89** (C3), 3689–3704, doi:
644 10.1029/JC089iC03p03689, URL <http://dx.doi.org/10.1029/JC089iC03p03689>.

645 Woodruff, S. D., and Coauthors, 2011: ICOADS Release 2.5: Extensions and enhancements to the
646 surface marine meteorological archive. *International Journal of Climatology*, **31** (7), 951–967,
647 doi:10.1002/joc.2103, URL <http://dx.doi.org/10.1002/joc.2103>.

648 Yueh, S., W. Tang, A. Fore, G. Neumann, A. Hayashi, A. Freedman, J. Chaubell, and G. Lager-
649 loef, 2013: L-band passive and active microwave geophysical model functions of ocean surface
650 winds and applications to Aquarius retrieval. *Geoscience and Remote Sensing, IEEE Transac-
651 tions on*, **51** (9), 4619–4632, doi:10.1109/TGRS.2013.2266915.

652 **LIST OF TABLES**

| | | | |
|-----|-----------------|---|----|
| 653 | Table 1. | Bias (before applying offsets) and root-mean-square error (after applying off- | |
| 654 | | sets), in K, of clear-sky, nearly-calm wind ($< 3.5 \text{ m s}^{-1}$) simulated brightness | |
| 655 | | temperatures forced with buoy observations of SST and 10m wind and MERRA | |
| 656 | | atmospheric parameters. No offsets were applied to the 183 GHz channels. | 33 |
| 657 | Table 2. | Root-mean-square error and bias of ensemble-mean deconvolved GPM Mi- | |
| 658 | | crowave Imager (GMI) radiances before and after filtering. | 34 |

659 TABLE 1. Bias (before applying offsets) and root-mean-square error (after applying offsets), in K, of clear-
660 sky, nearly-calm wind ($< 3.5 \text{ m s}^{-1}$) simulated brightness temperatures forced with buoy observations of SST
661 and 10m wind and MERRA atmospheric parameters. No offsets were applied to the 183 GHz channels.

| | FASTEM4 | | FASTEM5 | | Meissner-Wentz | |
|-------------|---------|------|---------|------|----------------|------|
| Channel | bias | rmse | bias | rmse | bias | rmse |
| 10.65V | 1.6 | 0.8 | 0.6 | 0.7 | -1.0 | 0.7 |
| 10.65H | 2.9 | 0.9 | -0.4 | 0.9 | -0.7 | 0.9 |
| 18.7V | 0.6 | 1.0 | 0.2 | 1.0 | -0.5 | 1.0 |
| 18.7H | 2.3 | 1.6 | 0.3 | 1.5 | 0.1 | 1.5 |
| 23.8V | -0.5 | 1.5 | -0.5 | 1.4 | -0.6 | 1.4 |
| 36.64V | 0.6 | 0.9 | 0.6 | 0.9 | 0.6 | 0.9 |
| 36.64H | 2.9 | 1.6 | 2.1 | 1.6 | 1.3 | 1.5 |
| 89V | -0.4 | 1.0 | 0.0 | 1.0 | 0.8 | 1.1 |
| 89H | 1.5 | 2.2 | 2.5 | 2.2 | 1.7 | 2.2 |
| 166V | -0.1 | 1.4 | -0.3 | 1.4 | -0.3 | 1.4 |
| 166H | 0.1 | 2.8 | 0.2 | 3.1 | 0.3 | 3.2 |
| 183 \pm 3 | -2.8 | 3.7 | -2.8 | 3.6 | -3.0 | 3.6 |
| 183 \pm 7 | -0.7 | 1.8 | -0.9 | 1.9 | -1.0 | 1.9 |

662 TABLE 2. Root-mean-square error and bias of ensemble-mean deconvolved GPM Microwave Imager (GMI)
663 radiances before and after filtering.

| | 10V | 10H | 18V | 18H | 23V | 36V | 36H | 89V | 89H |
|------------------|------|------|------|-------|------|------|-------|-------|-------|
| Initial rmse (K) | 6.7 | 11.3 | 11.6 | 19.8 | 12.0 | 15.5 | 26.6 | 23.1 | 25.9 |
| Initial Bias (K) | -3.7 | -7.2 | -6.0 | -10.9 | -6.5 | -9.0 | -14.3 | -16.1 | -16.0 |
| NS rmse (K) | 4.6 | 7.1 | 7.2 | 11.1 | 8.1 | 9.9 | 15.1 | 16.2 | 16.9 |
| NS Bias (K) | -1.7 | -3.6 | -2.9 | -5.0 | -3.3 | -4.8 | -5.7 | -11.6 | -8.2 |
| MS rmse (K) | 8.1 | 9.8 | 11.1 | 15.1 | 12.7 | 13.6 | 20.0 | 22.0 | 24.8 |
| MS Bias (K) | -2.5 | -4.0 | -4.4 | -6.8 | -5.2 | -5.9 | -8.4 | -13.2 | -12.5 |

| | | |
|-----|------------------------|---|
| 664 | LIST OF FIGURES | |
| 665 | Fig. 1. | Flow chart of the process by which the DPR geophysical model function (GMF) is derived and used by the combined DPR-GMI precipitation algorithm. 36 |
| 666 | | |
| 667 | Fig. 2. | MERRA and GMI-retrieved wind speed bias relative to ICOADS buoy observations from March-December 2014. Error bars represent 1 standard deviation of the difference between observed and retrieved wind speeds in each bin. 37 |
| 668 | | |
| 669 | | |
| 670 | Fig. 3. | Standard deviation of σ_0 in three wind speed bins: 0.5 m s^{-1} (top), 5 m s^{-1} (middle), and 15 m s^{-1} (bottom). The different colors represent different frequencies, DPR modes (NS = Normal Scan, MS = Matched Scan, HS = High Sensitivity), and quality control of the reference wind. 38 |
| 671 | | |
| 672 | | |
| 673 | | |
| 674 | Fig. 4. | The two-dimensional geophysical model functions (GMFs) of σ_0 , its standard deviation, Ku-Ka correlation, and difference between the Durden-Vesecky single-amplitude model and observations at Ku band are shown as a function of 10m wind speed and incidence angle. 39 |
| 675 | | |
| 676 | | |
| 677 | Fig. 5. | False-color GMI composite and KuPR maximum column observed reflectivity at 2204 UTC 26 January 2015. The GMI composite is from the 89 GHz V and H and 36 GHz V channels following the Negri et al. (1989) scheme. 40 |
| 678 | | |
| 679 | | |
| 680 | Fig. 6. | Correlations of Ku and Ka σ_0 and 10.65, 18.7, and 36.6 GHz horizontally-polarized brightness temperatures to surface rain rate and 10m wind speed, derived from the initial ensemble of solutions to each radar profile. 41 |
| 681 | | |
| 682 | | |
| 683 | Fig. 7. | Root-mean-square error (a) and bias (b) of the initial and filtered ensemble mean σ_0 as a function of incidence angle. 42 |
| 684 | | |
| 685 | Fig. 8. | Background (JMA Global Analysis GANAL; 2A-ENV) and retrieved wind root-mean-square error and bias relative to ICOADS buoy observations in precipitating pixels. 43 |
| 686 | | |
| 687 | Fig. 9. | Retrieved wind root mean square error as a function of DPR incidence angle. The data are smoothed using a 7-bin centered average in order to reduce noise from the small sample size in each angle bin. 44 |
| 688 | | |
| 689 | | |
| 690 | Fig. 10. | Change in GPM combined algorithm precipitation, as a function of wind speed and incidence angle, when the Surface Reference Technique (SRT) path-integrated attenuation (PIA) is replaced with the observed σ_0 in the observation vector and coupled σ_0 -emissivity model is used in the forward model. The ENV wind and SRT-based precipitation are used as reference values. 45 |
| 691 | | |
| 692 | | |
| 693 | | |
| 694 | | |

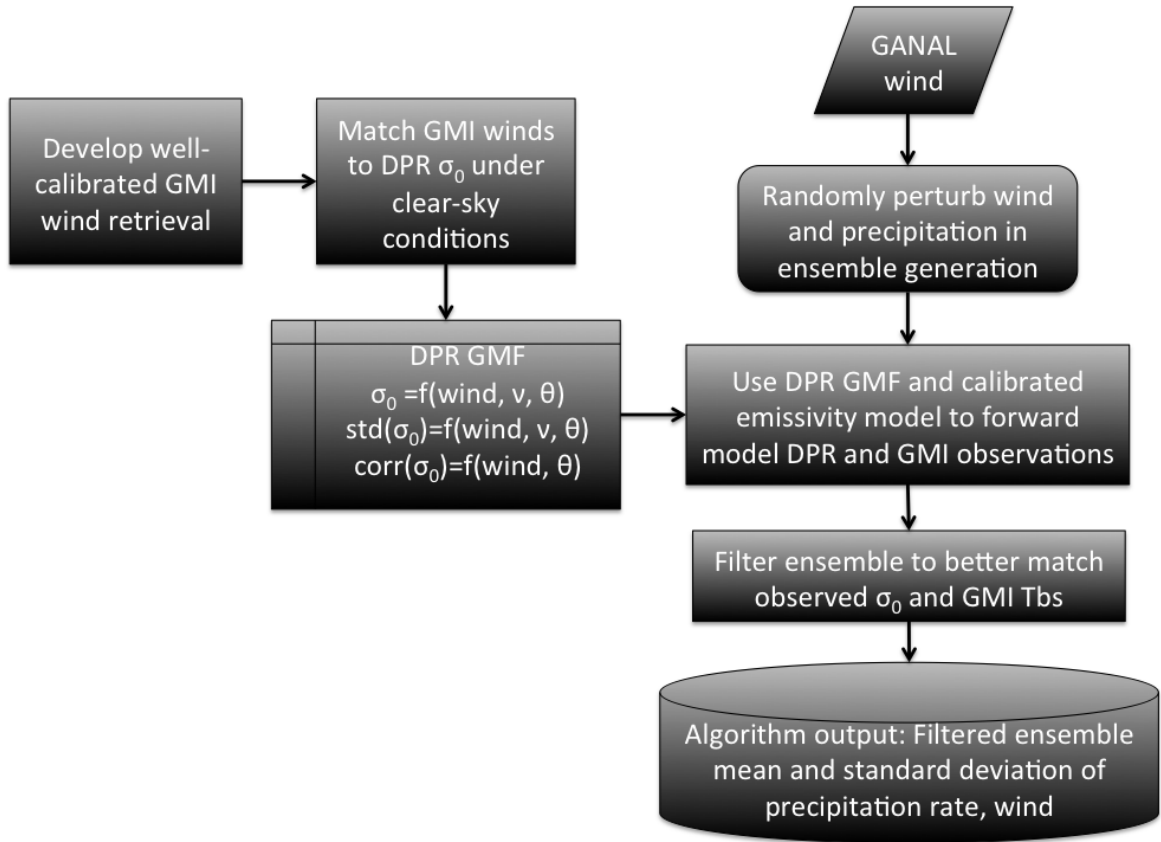


FIG. 1. Flow chart of the process by which the DPR geophysical model function (GMF) is derived and used by the combined DPR-GMI precipitation algorithm.

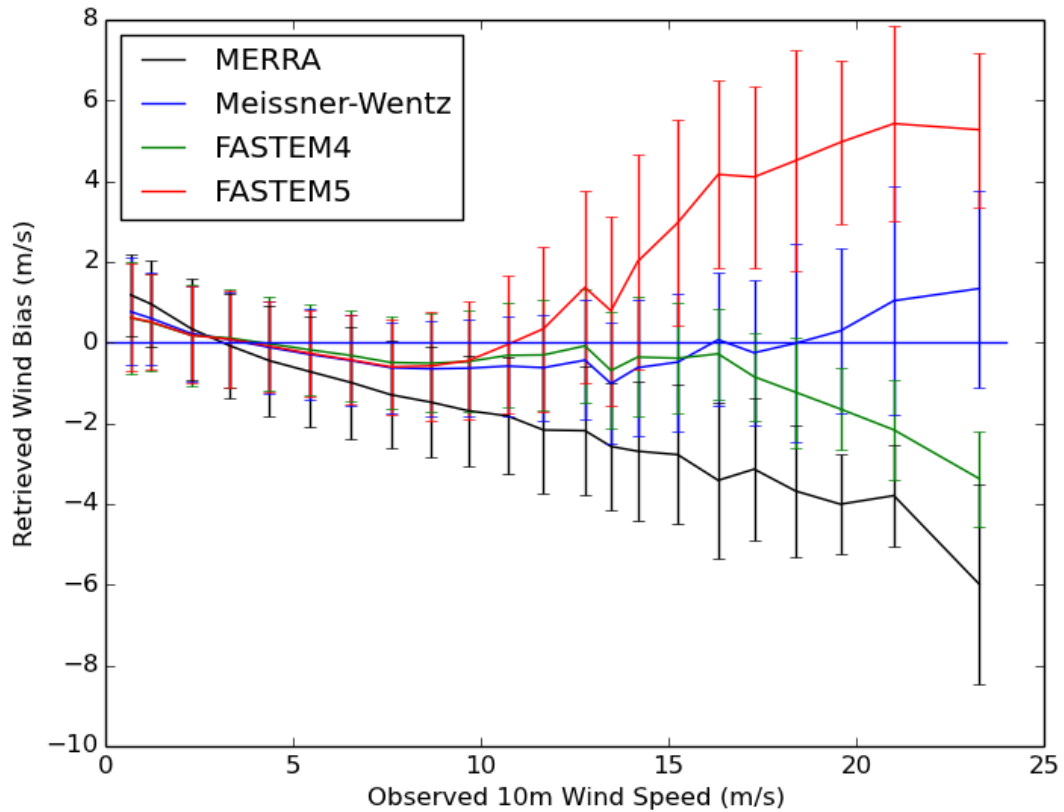


FIG. 2. MERRA and GMI-retrieved wind speed bias relative to ICOADS buoy observations from March-December 2014. Error bars represent 1 standard deviation of the difference between observed and retrieved wind speeds in each bin.

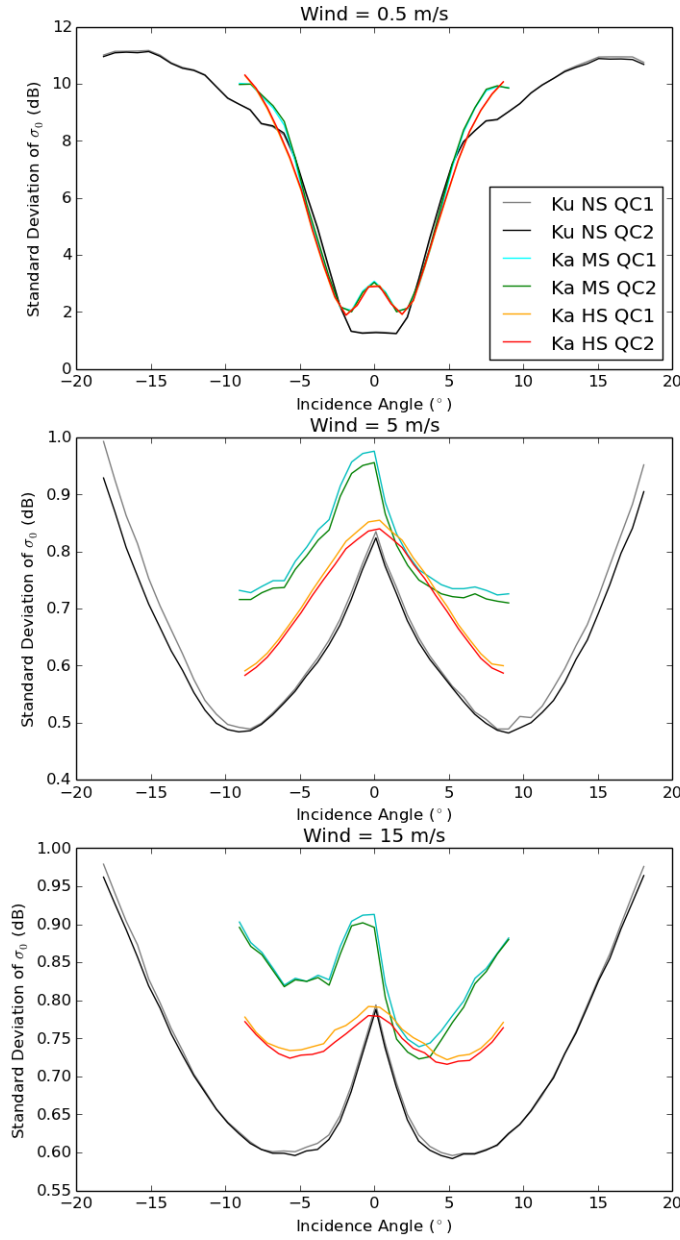


FIG. 3. Standard deviation of σ_0 in three wind speed bins: 0.5 m s^{-1} (top), 5 m s^{-1} (middle), and 15 m s^{-1} (bottom). The different colors represent different frequencies, DPR modes (NS = Normal Scan, MS = Matched Scan, HS = High Sensitivity), and quality control of the reference wind.

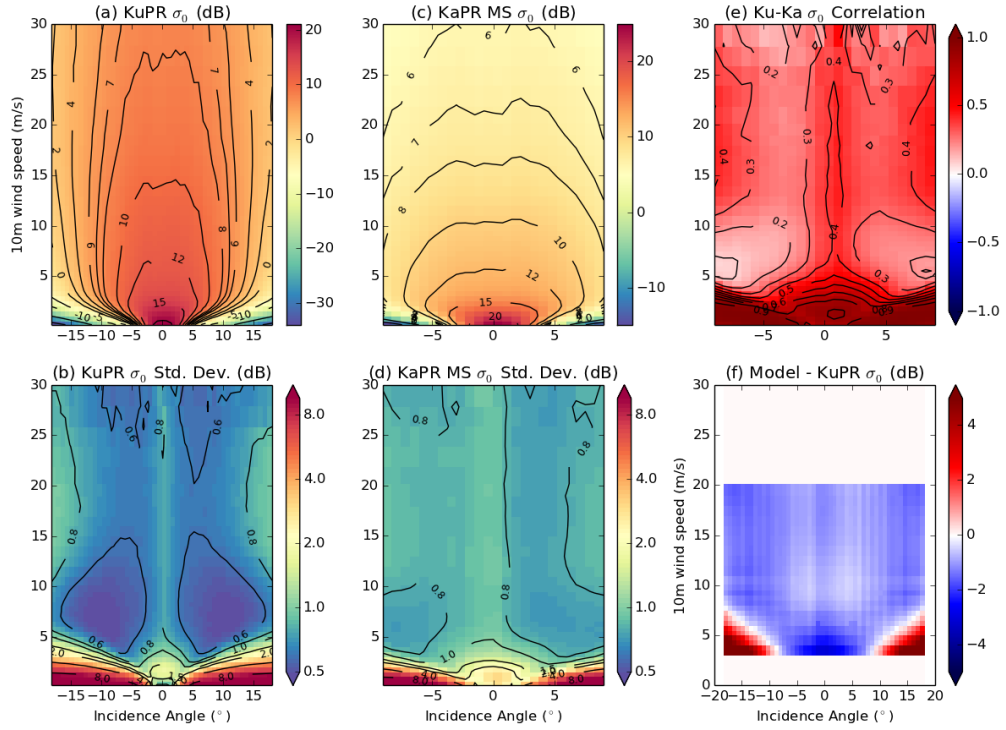


FIG. 4. The two-dimensional geophysical model functions (GMFs) of σ_0 , its standard deviation, Ku-Ka correlation, and difference between the Durden-Vesecky single-amplitude model and observations at Ku band are shown as a function of 10m wind speed and incidence angle.

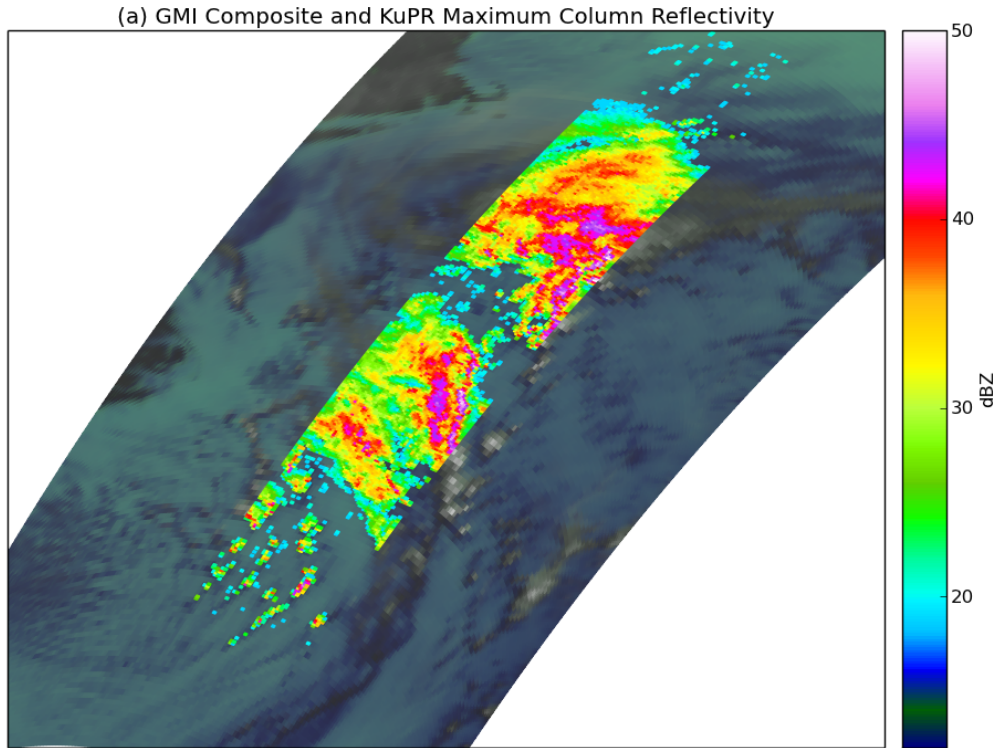


FIG. 5. False-color GMI composite and KuPR maximum column observed reflectivity at 2204 UTC 26
January 2015. The GMI composite is from the 89 GHz V and H and 36 GHz V channels following the Negri
et al. (1989) scheme.

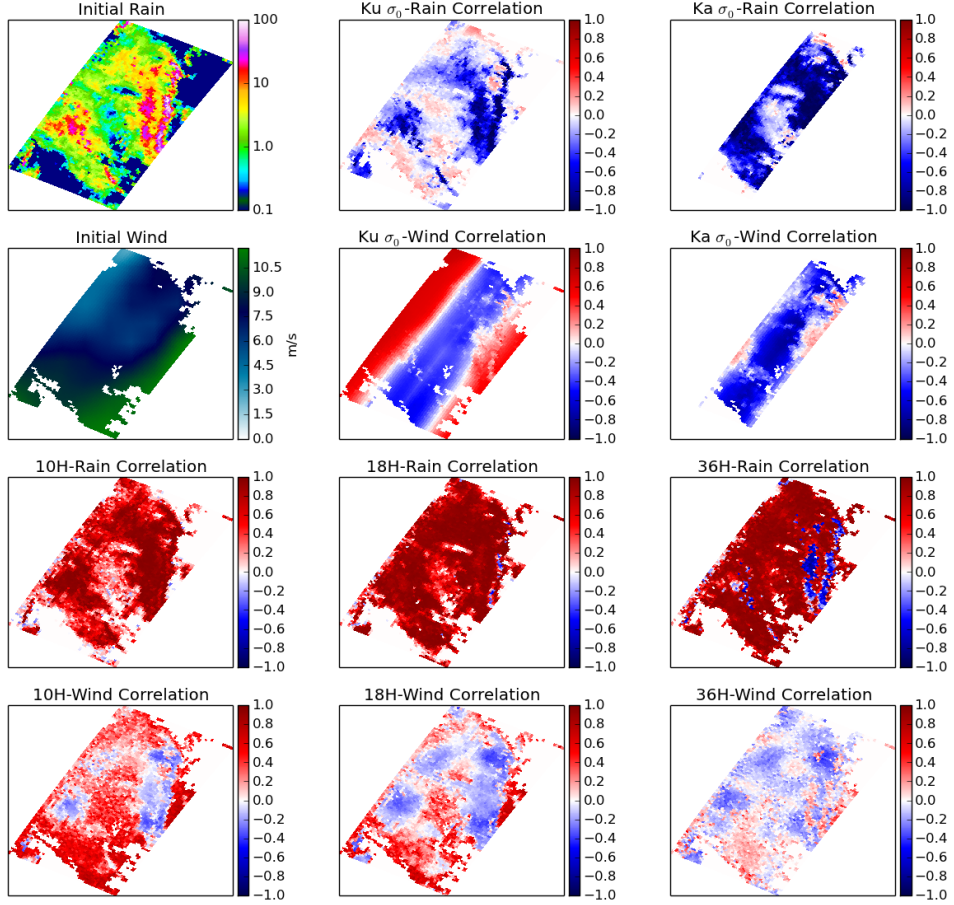


FIG. 6. Correlations of Ku and Ka σ_0 and 10.65, 18.7, and 36.6 GHz horizontally-polarized brightness temperatures to surface rain rate and 10m wind speed, derived from the initial ensemble of solutions to each radar profile.

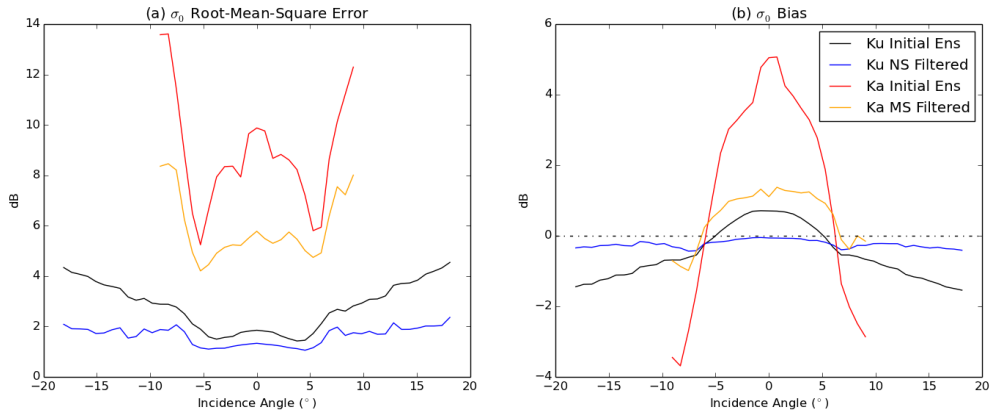


FIG. 7. Root-mean-square error (a) and bias (b) of the initial and filtered ensemble mean σ_0 as a function of incidence angle.

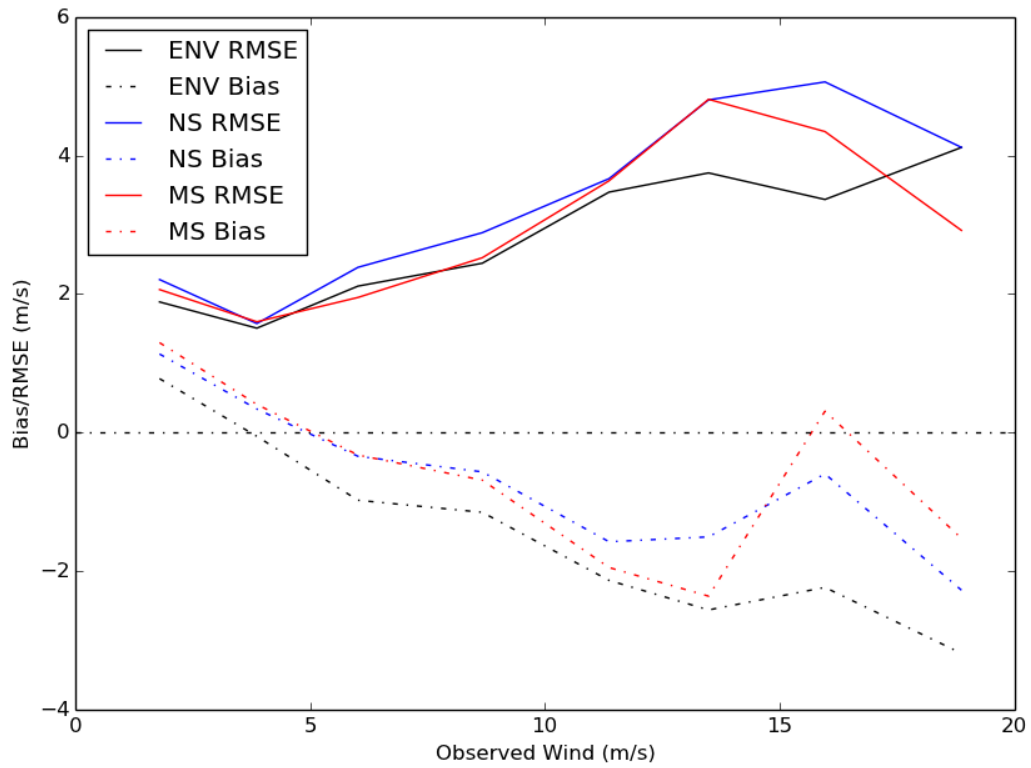


FIG. 8. Background (JMA Global Analysis GANAL; 2A-ENV) and retrieved wind root-mean-square error and bias relative to ICOADS buoy observations in precipitating pixels.

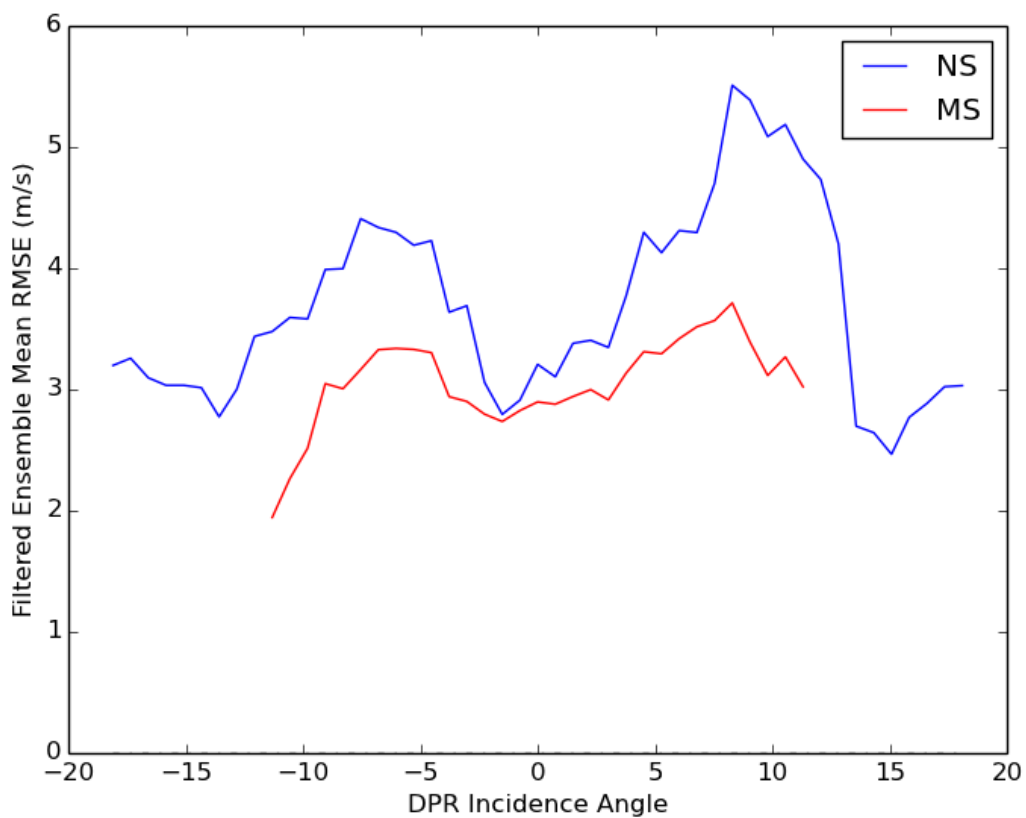
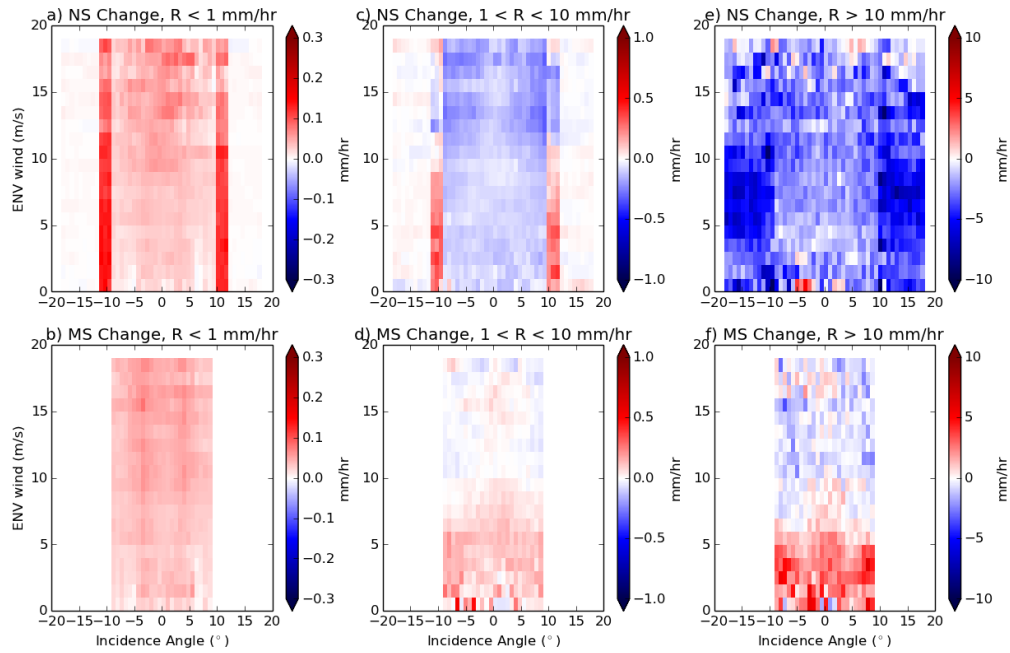


FIG. 9. Retrieved wind root mean square error as a function of DPR incidence angle. The data are smoothed using a 7-bin centered average in order to reduce noise from the small sample size in each angle bin.



718 FIG. 10. Change in GPM combined algorithm precipitation, as a function of wind speed and incidence angle,
 719 when the Surface Reference Technique (SRT) path-integrated attenuation (PIA) is replaced with the observed
 720 σ_0 in the observation vector and coupled σ_0 -emissivity model is used in the forward model. The ENV wind and
 721 SRT-based precipitation are used as reference values.